Invited paper

Limin Wu, Weiwei Guo, Xiaofu Sun* and Buxing Han*

Rational design of nanocatalysts for ambient ammonia electrosynthesis

https://doi.org/10.1515/pac-2021-0204

Abstract: Ammonia (NH_3) is one of the key commercial chemicals and carbon-free energy carriers. It is mainly made by Haber-Bosch process under high temperature and high pressure, which consumes huge amount of energy and releases large amounts of CO_2. Developing sustainable approaches to its production is of great importance. Powered by a renewable electricity source, electrochemical N_2 reduction reaction (NRR) and nitrate reduction reaction (NITRR) are potential routes to synthesize NH_3 under ambient conditions. This review summarizes major recent advances in the NRR and NITRR, especially for several years. Some fundamentals for NRR and NITRR are first introduced. Afterward, the design strategies of nanocatalysts are discussed, mainly focusing on nano-structure construction/nanoconfinement, doping/defects engineering and single-atom engineering. Finally, the critical challenges remaining in this research area and promising directions for future research are discussed.

Keywords: Catalysis; Green Chemistry; 2019 IUPAC-Zhejiang NHU International Award.

Introduction

As one of the basic chemicals, ammonia (NH_3) is widely used in the agriculture and chemical industry as an upstream reagent for producing value-added chemicals, such as fertilizers, medicines, dyes, fuels and explosives [1]. NH_3 is also considered as a replacement of hydrogen due to its hydrogen density of 17.8 % [2]. It has attracted great attention as an effective carbon-free energy carrier and a crucial CO_2 free transportation fuel. Currently, the industrial NH_3 synthesis is mainly produced via the Haber-Bosch process, which is viewed as one of the greatest inventions of the 20th century and contributes 90 % of annual production [3]. However, the sluggish kinetics of the reaction between N_2 and H_2 requires high temperatures (300–600 °C) and pressures (15–40 MPa), thus consuming a large amount of energy. As a result, the overall process not only accounts for 1–2 % of the total global energy consumption, but also releases about 400 Mt of CO_2 every

Article note: A collection of peer-reviewed articles by the winners of the 2019 IUPAC-Zhejiang NHU International Award for Advancements in Green Chemistry.

***Corresponding authors: Xiaofu Sun**, Beijing National Laboratory for Molecular Sciences, CAS Key Laboratory of Colloid and Interface and Thermodynamics, CAS Research/Education Center for Excellence in Molecular Sciences, Institute of Chemistry, Chinese Academy of Sciences, Beijing, 100190, China; and School of Chemistry and Chemical Engineering, University of Chinese Academy of Sciences, Beijing, 100049, China, e-mail: sunxiaofu@iccas.ac.cn; and **Buxing Han**, Beijing National Laboratory for Molecular Sciences, CAS Key Laboratory of Colloid and Interface and Thermodynamics, CAS Research/Education Center for Excellence in Molecular Sciences, Institute of Chemistry, Chinese Academy of Sciences, Beijing, 100190, China; School of Chemistry and Chemical Engineering, University of Chinese Academy of Sciences, Beijing, 100049, China; and Shanghai Key Laboratory of Green Chemistry and Chemical Processes, School of Chemistry and Molecular Engineering, East China Normal University, Shanghai, 200062, China, e-mail: hanbx@iccas.ac.cn.

Limin Wu and Weiwei Guo, Beijing National Laboratory for Molecular Sciences, CAS Key Laboratory of Colloid and Interface and Thermodynamics, CAS Research/Education Center for Excellence in Molecular Sciences, Institute of Chemistry, Chinese Academy of Sciences, Beijing, 100190, China; and School of Chemistry and Chemical Engineering, University of Chinese Academy of Sciences, Beijing, 100049, China

© 2021 IUPAC & De Gruyter. This work is licensed under a Creative Commons Attribution-NonCommercial-NoDerivatives 4.0 International License. For more information, please visit: http://creativecommons.org/licenses/by-nc-nd/4.0/

year [4]. Considering the huge energy and environment costs, it is desirable to develop green and sustainable strategy to achieve highly efficient NH_3 synthesis under ambient conditions.

In recent years, electrocatalytic reduction method has received much interest for NH_3 production. It is an environmentally benign and ideal method, which can be performed in simple reaction units under ambient conditions via renewable energy such as solar and wind without emitting CO_2. In the meantime, electrochemical method also offers an approach for converting renewable electricity into chemicals or chemical energy directly. NH_3 is increasingly recognized as a highly viable chemical energy carrier. As a result, NH_3 electrosynthesis under ambient conditions is attracting increasing attention in recent years with a focus on the two principal reaction processes: N_2 reduction reaction (NRR) and nitrate reduction reaction (NITRR).

N_2 is the main component of air and the cheapest nitrogen source. N_2 is usually viewed as a chemically inactive gas due to its extremely stable nature under normal conditions. In fact, elemental nitrogen has high chemical activity and high electronegativity (3.04), indicating that it can form strong bonds with other elements. However, N_2 is chemically inert due to its strong N≡N triple bond (941 $kJ \cdot mol^{-1}$), high thermodynamic stability, lack of dipole moment and low polarizability [5]. Therefore, the optimal conditions for activation of N_2 molecules at room temperature and atmospheric pressure have not been achieved.

A massive amount of nitrate exists in the biosphere and the concentration of environmental nitrate increases over time due to human activities, such as the combustion of N-containing fossil fuels, the discharge of industrial waste water, and the bacterial decomposition of fertilizers. The accumulation of nitrate causes serious illnesses and threatens human health. On the other hand, nitrate is also a prospective nitrogen source for the production of NH_3. The activation of nitrate is much easier than that of N_2, and thus adopting nitrate as a raw material to prepare NH_3 is a promising route.

The prerequisite steps for NRR and NITRR are the chemisorption of N_2 or nitrate onto the active sites and the following activation with receiving electron from the catalysts. Increasing the quantity of active sites and intrinsic activity of each active site can improve the catalytic performance [6]. NRR occurs at solid-gas-liquid interfaces while NITRR happens at solid-liquid interfaces. The main challenge is to minimize the primary competing reaction-hydrogen evolution reaction (HER), which determines the selectivity of NH_3 production [7]. Therefore, one of the challenges in this field is to develop selective and efficient electrocatalysts to achieve superior catalytic activity and selectivity for NH_3 synthesis at low overpotentials. Over the past few decades, many catalysts have been evaluated for NH_3 electrosynthesis, including metals, metal oxides, metal complexes and metal-free electrodes. Some design strategies, such as nano-structure construction/nanoconfinement, doping/defects engineering and single-atom engineering, have been developed to overcome the kinetic limitations of NRR or NITRR and significantly decrease the reaction overpotential.

The heterogeneous reaction catalyzed by porous materials of nanometer scale often presents higher activity and selectivity, which is also called nanoconfinement effects [8]. Nano-structure construction and nanoconfinement effects change the motion characteristics of electrons, leading to the change of electronic structure, especially for the valence electron structure [9]. Doping and defects are common in the preparation of catalysts, which can provide more active sites to promote the occurrence of catalytic reactions [10]. Doping atoms can promote charge transfer and improve the electrical conductivity [11]. Defects are widely used in electrocatalysts to regulate the properties of the surfaces/interfaces [12]. Doping and defects engineering can reduce the apparent activation energy, produce more active unsaturated atoms and significantly affect the electronic structure. Single-atom catalysts possess atomically dispersed metal active sites, which plays an important role in overcoming the limitations of nanoparticles and bulk materials during the catalytic process [13, 14]. Due to the unique electronic structure and high atomic utilization ratio, single-atom catalysts are considered to combine the best properties of a variety of catalysts: high stability, high utilization efficiency, high catalytic activity, high reaction selectivity, uniform structural model, and ease of separation [15]. These design strategies have been widely applied in other electrocatalytic systems, such as HER, oxygen evolution reaction (OER), oxygen reduction reaction (ORR) and CO_2 reduction reaction [16, 17], which provides a reference for the development of novel catalysts for NRR and NITRR.

Herein, we systematically review recent progress on the design of nanocatalysts for ambient NRR and NITRR (Fig. 1). First, we commence with the fundamental parameters for NRR and NITRR activity evaluation, followed by the introduction of reaction mechanisms to guide the rational design of high performance electrocatalysts. Second, the method of the identification and elimination of false positives for NH_3 electrosynthesis are presented. Afterward, the design strategies of nanocatalysts for NRR and NITRR with emphasis on the active sites and intrinsic elucidation are discussed in detail, mainly including nano-structure construction/nanoconfinement, doping/defects engineering and single-atom engineering. In addition, the remaining challenges and some perspectives for NRR and NITRR are provided in the final section.

Fundamentals of NH_3 electrosynthesis

Useful parameter in NH_3 electrosynthesis

With respect to the evaluation and comparison of the catalytic performance for NH_3 electrosynthesis, it is necessary to clarify the definitions of several fundamental parameters.

1) Faraday efficiency (FE)

FE is a common term in electrochemical fields, which can be understood as the percentage of actual and theoretical products. The FE of the desired product produced by the electrocatalyst at different voltages has become an important index to investigate the electrocatalytic performance of the catalyst. In NH_3 electrosynthesis, FE reflects the selectivity for NH_3 formation. It is influenced by temperature, applied voltage, electrolyte type and concentration, solution acidity and electrocatalyst.

FE is calculated according to the equation as follows,

$$FE = nF \times [NH_3] \times V/(17 \times Q) \quad (1)$$

where n is the number of electrons transferred, F is the Faraday constant, V is the total volume of electrolyte in cathodic compartment, and Q is the total charge passed through the electrodes.

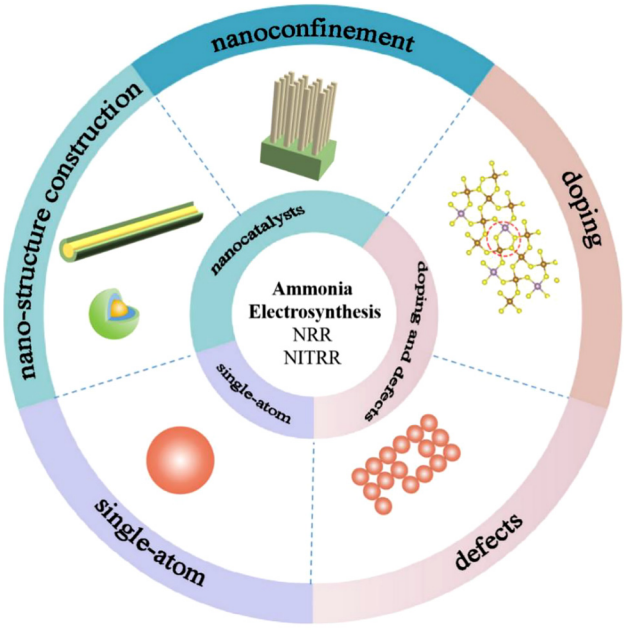

Fig. 1: Diagram of the design of electrocatalysts with distinctive active sites and structures.

2) NH_3 yield and evolving rate (νNH_3)
NH_3 yield and νNH_3 can be obtained by using the following equations.

$$NH_3 \text{ yield} = ([NH_3] \times V)/(t \times A) \tag{2}$$

$$\nu_{NH3} = ([NH_3] \times V)/(t \times m) \tag{3}$$

where t is the reaction time, A is the surface area of working electrode, and m is the catalyst mass [18, 19].
3) Current density
The current density is a measure of the reaction rate and typically calculated via dividing the current by the geometric surface area of the working electrode. It usually determines the electrolyzer size and the cost needed, so it is important for the practical applications. The partial current density for NH_3 can be acquired by multiplying the corresponding FE by the current density.
4) Overpotential (η)
Overpotential is the potential difference between the thermodynamically determined reduction potential of the half reaction and the experimentally observed potential of the redox reaction. That is, $\eta = E - E_{eq}$. It is very useful in evaluating the performance of electrocatalysts. A smaller overpotential indicates better catalytic performance.
5) Stability and cycle number
Stability is a significant and necessary parameter of catalysts. The chrono-amperometry results and the cycling stability in multiple experiments should be usually provided.

Reaction mechanism of NH_3 electrosynthesis

For NRR, after the initial N_2 chemisorption and activation steps, the subsequent reactions involve a number of complex electron transfer and hydrogenation processes. In general, NRR on a heterogeneous surface can be divided into two mechanisms: the dissociative and associative pathways as is shown in Fig. 2 [20]. In the dissociative mechanism, N≡N bonds are broken by reduction before the protonation step. After N≡N is broken, the N atoms on the surface of the isolated catalyst are converted to NH_3 by hydrogenation. However, N-N bonds remain intact in some or most of the reduction steps in the associative mechanism. According to the hydrogenation sequence, the associative pathways are divided into alternating pathway and distal pathway. Two N atoms react with protons at the same time in the associative alternating pathway, which may lead to the production of by-products such as N_2H_4. For the associative distal pathway, the terminal N atoms preferentially participate in the hydrogenation reaction. Once the distal NH_3 molecule is released, proton addition occurs on its surface N atoms. By this pathway, only NH_3 can be formed, while other byproducts are not produced.

According to the equation as follows, NITRR is a complicated multi-electron-transfer process involving different nitrogen-containing species from +5 to −3 valence states [21]. Nitrate reduction to NH_3, which needs three more electrons than nitrate reduction to N_2, is much easier according to no N-N bond needs to be formed. For NITRR, the process is the conversion of NO_3^- into NH_3 through deoxygenation ($N{-}O_3 \rightarrow N{-}O_2 \rightarrow N{-}O$) and hydrogenation ($N{-}O \rightarrow H{-}N{-}O \rightarrow H_2{-}N{-}O \rightarrow N{-}H_2 \rightarrow N{-}H_3$) steps (see Fig. 3).

$$NO_{3^-} + 9H^+ + 8e^- \rightarrow NH_3 + 3H_2\ E° = 0.12\,V \text{ vs. standard hydrogen electrode (SHE)} \tag{4}$$

Identification in NH_3 electrosynthesis

Though a growing number of researchers are paying attention to the NRR and NITRR, there are still various puzzling questions to be solved. Three critical questions were put forward by Choi and other partners are

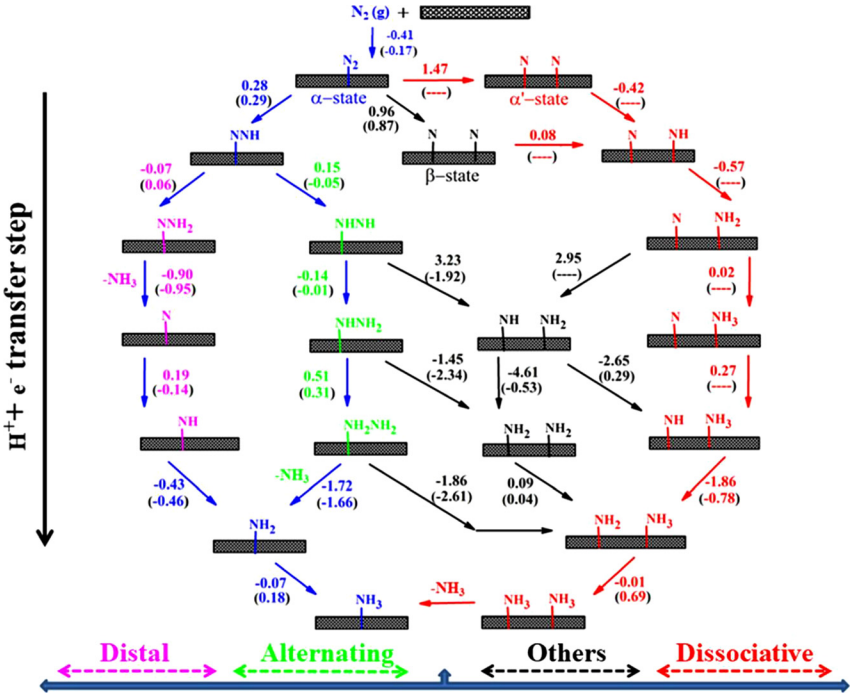

Fig. 2: Reaction Intermediates for Associative and Dissociative NRR with ΔG Values on the Periodic Fe (111) Surface and $Fe_{55}NC$[a]. Reprinted with permission from Ref. [21]. Copyright 2020 American Chemical Society.

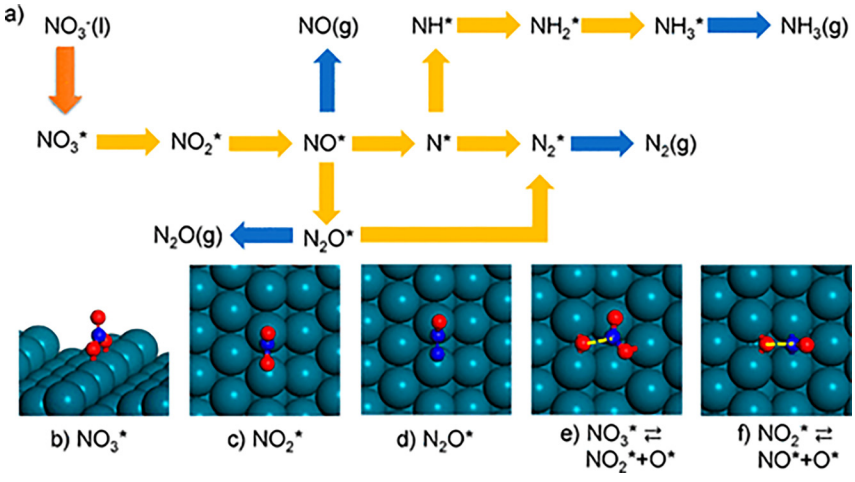

Fig. 3: The electron-mediated pathway of nitrate electroreduction. Reprinted with permission from Ref. [21]. Copyright 2019 American Chemical Society.

as following. Are NH_3 yield rate high enough? Are the experiments conducted using $^{15}N_2$ reliable and sufficient to confirm the key results? Is the control and quantification of NO_x that may exist in the experiment strict enough [22]?

It is highly plausible and promising when NH_3 yield rate is higher than 10 nmol s^{-1} cm^{-2}. However, although many kinds of excellent catalysts have been applied to promote NH_3 production, the amount of NH_3 is so small that it cannot be firmly identified that NH_3 comes from electrocatalytic reactions. The presence of

false positives has a bad effect on the reaction, especially for the NRR. Contamination from NH_3 mainly comes from two aspects: on the one hand, NH_3 may exist in air, human breath or ion-conducting membranes. on the other hand, there are unstable N-containing compounds in the nitrogen gas stream, electrolyte and even catalyst. It is of critical necessity to operate on a number of control experiments to verify that the NH_3 is not contaminated by reactants, instrument or environment. There are mainly three kinds of control experiments: 1) an Ar-saturated electrolyte that N_2 is replaced by Ar is applied; 2) blank reactions without current input is carried out; 3) a bare carbon paper is regarded as an electrode. Without generating detectable amounts of NH_3 in the above experiments, the experimental apparatus, the N_2 gas, and the catalyst are verified not be contaminated by activated nitrogen or NH_3. A linear increase in content with the amount of electricity further indicates that NH_3 in the electrolyte is the result of the electroreduction of N_2 [23]. Nitrate and nitrite contamination can be detected by simple spectrophotometric methods or Nuclear Magnetic Resonance Spectroscopy (NMR) and can be removed by high temperature treatment [24].

The pH of the reaction medium varies considerably in electrocatalysis, and NH_3 detection methods need to be properly selected. It is of great benefits for accuracy of results to use multiple detection methods. Nessler's reagent method, indophenol blue method, and ion chromatography method are all accurate when the concentrations of NH_3 are less than 500 μg L^{-1}. Nessler's reagent method and ion chromatography are more suitable to be applied in acidic media. Nessler's reagent method, indophenol blue method inclined to be used in alkaline media. All the three methods can be adopted as detection methods in neutral media [25].

Strategies for the design of nanocatalysts

Despite of the progress achieved for NH_3 Electrosynthesis to date, the performance of the current NRR or NITRR catalysts is far from satisfactory. The volcano plot reveals a close interconnectedness between the intrinsic adsorption property of the catalyst surface and its apparent catalytic activity. Therefore, it is very urgent to adjust the "moderate degree" adsorption strength of the catalysts.

The design of nanocatalysts for NRR

Nano-structure construction and nanoconfinement

Recently, CoMoC nanoporous catalysts [26], $FeMo_3S_4$ nanorods [27], FeMoO4 nanorods [28], CrN nanocube [29], $Fe_2(MoO_4)_3$ nanoparticles [30], molybdenum nitride (MoN_2) nanosheet [31], three-dimensional Pd-Ag-S porous nanosponges [32], two-dimensional MXenes [33], MoO2 nanoparticles supported by carbon nanowires [34], Au nanocrystals [35], bimetallic Au-Ag nanocages [36], NiCoS/C nanocages [37], AuPdP Nanowires [38], amorphous $CoMoO_4$ catalysts with nanoporous structures [39], palladium nanothorn assembly array [40], VN nanowire array on carbon cloth [41] and nanorod-structured MoN [42] have been used as efficient for NRR under ambient conditions. It indicated that nano-structure construction and nanoconfinement are efficient method for the design of electrocatalysts for NRR.

Nazemi et al. [43] enhanced the rate of NRR by the design of hollow Au nanocages (AuNCs). It achieved the highest FE of 30.2 % and the highest yield rate of 3.9 μg cm^{-2} h^{-1} in 0.5 M $LiClO_4$ aqueous solution. Compared with Au nanocubes, nanospheres, and nanorods, the AuNCs had the highest catalytic efficiency. The increased amount of valency-unsatisfied surface atoms with sharper edges and corners of AuNCs provided much more active sites for NRR. On the other hand, the increasing surface area and confinement of reactants in the cavity extended the residence time of N_2 molecules on the nanoparticle inner surface.

Li et al. [44]. reported that the dendritic Cu was a high-efficiency electrocatalyst for NRR with a high NH_3 yield rate of 25.63 μg mg^{-1} h^{-1} and a FE of 15.12 % at −0.4 V vs. RHE in 1 M HCl electrolyte. The dendritic Cu nanostructures with rich orientation tips and high surface area can serve as an efficient electrocatalyst. The

spikes on the material surface significantly amplified the local electric field, leading to improvement of reagent concentration near electrode tips [45, 46]. This special structure greatly facilitated the interaction between electrocatalysts and reactants by providing a great number of active sites.

Xue et al. [47] reported an efficient NRR catalyst that was composed of the donor-acceptor couples of Ni and Au nanoparticles supported on nitrogen-doped carbon. It can achieve a maximum NH_3 production rate of 7.4 μg h^{-1} mg^{-1} with a high Faradaic efficiency of 67.8 % at −0.14 V vs. RHE. It is worth noting that Au_6/Ni is superior to the other electrocatalysts with various atomic ratios of the Au-Ni couples and Au- [48], Ru- [49], or Pd-based [50] electrocatalysts. The highly coupled Au and Ni nanoparticles loaded on carbon make the catalyst have long-term and reusable NRR stability, leading to the electrochemical processes more sustainable in practical applications. From the experimental and theoretical results, it can be known that the as-formed electron-rich Au species can accept electrons from Ni species, and thus facilitating the adsorption, activation and dissociation of N_2 molecule. The work gave a guideline for the fabrication of electrocatalysts for NRR via the construction of metal-metal donor-acceptor couples.

Pd-Ru bimetallic porous nanostructures (Pd-Ru BPNs) were used as electrocatalysts for NRR with a FE of 1.53 % at −0.1 V in 0.1 M HCl and prominent stability. A high NH_3 yield rate of 25.92 μg mg^{-1} h^{-1} was obtained, which was 4.2 times higher than that of monometallic Pd and 2.5 times than that of monometallic Ru (Fig. 4) [51]. The scanning electron microscopy (SEM) image of Pd-Ru BPNs revealed that it consisted of porous structures with interconnected networks (Fig. 4(a)). The transmission electron microscope (TEM) further supported that the morphology of the Pd-Ru BPNs possessed fused architectures (Fig. 4(b)). As shown in Fig. 4(c), the average size of Pd-Ru BPNs was approximately 4–6 nm with well-defined crystal lattices which were detected by the high-resolution transmission electron microscopy (HRTEM). As shown in Fig. 4(d), the fast Fourier transform (FFT) patterns observed an interplanar spacing of 0.223 nm indexed to the (111) crystal plane of the PdRu BPNs. All above results indicated that Pd-Ru BPNs had been synthesized. Pd-Ru BPNs were prepared by the co-reduction of Pd and Ru precursors, and the coordination environments and electronic states of Pd and Ru can be also tailored by bimetallic nanostructures. The three-dimensional interconnected porous nanostructures did not only increase the number of active sites and enhanced the interaction of the adsorbed N species to facilitate NRR, but also effectively prevented the agglomeration of Pd-Ru to improve the long-term durability.

Shi et al. [52] anchored Pd–Cu amorphous nanoclusters on reduced graphene oxide (rGO), and the synergistic effects of the components in $Pd_{0.2}Cu_{0.8}$/rGO composites played a significant role in facilitating the electrocatalytic NRR performance. The NH_3 yield rate was 2.80 μg h^{-1} $mg_{cat}{}^{-1}$ at a low overpotential of −0.2 V vs. RHE. It was 2.1 times higher than Pd/rGO, 2.4 times higher than Cu/rGO and 3.2 times higher than $Pd_{0.2}Cu_{0.8}$/NPs. Pd can be used as a nitrogen-fixing catalyst, but Pd inclined to bind H adatoms compared with N ones. The introduction of Cu accelerated H desorption to prevent Pd from being covered by H. Compared with pure metal Pd or Cu, the bimetallic Pd–Cu increased the possibility of NRR. The electronic interaction between Pd and Cu also changed the electronic states of metal atoms and produced new catalytic centers obviously, and thus improving the catalytic activity. On the other hand, the dangling bonds on amorphous materials provided more active sites, which further increased the possibility of N_2 molecular activation. Furthermore, the addition of rGO support enhanced the dispersion of the catalytic sites, and improved N_2 molecules adsorption capacity.

The nanoporous palladium hydride (Pd–H) was also designed as electrocatalyst for NRR [53]. A high yield rate of 20.4 μg mg^{-1} h^{-1} and a high FE of 43.6 % for NH_3 production was achieved at −0.2 V vs. RHE in 0.1 M HCl. Compared with the pristine Pd, the NRR activity and selectivity of nanoporous Pd-H hydrides were significantly improved. The hydrogenation of Pd effectively altered the *d*-electron center and enhanced the catalytic activity. The study revealed that NH_3 was formed through the reaction of N adsorbed and H extracted from the outermost Pd–H lattice, and then H vacancies can be repaired by activating H_2O.

Cr_2O_3 was viewed as an excellent non-noble-metal catalyst for NRR. Cr_2O_3 nanofiber affords a high FE of 8.56 % and a high NH_3 formation rate of 28.13 μg h^{-1} $mg_{cat}{}^{-1}$ in 0.1 M HCl. Cr_2O_3 nanoparticle-reduced graphene oxide hybrid (Cr_2O_3-rGO) also showed excellent selectivity and stability for NH_3 synthesis with a high NH_3 yield (33.3 μg h^{-1} $mg_{cat}{}^{-1}$, −0.7 V (RHE)) and a high FE (7.33 %, −0.6 V (RHE)). Zhang et al. [54]

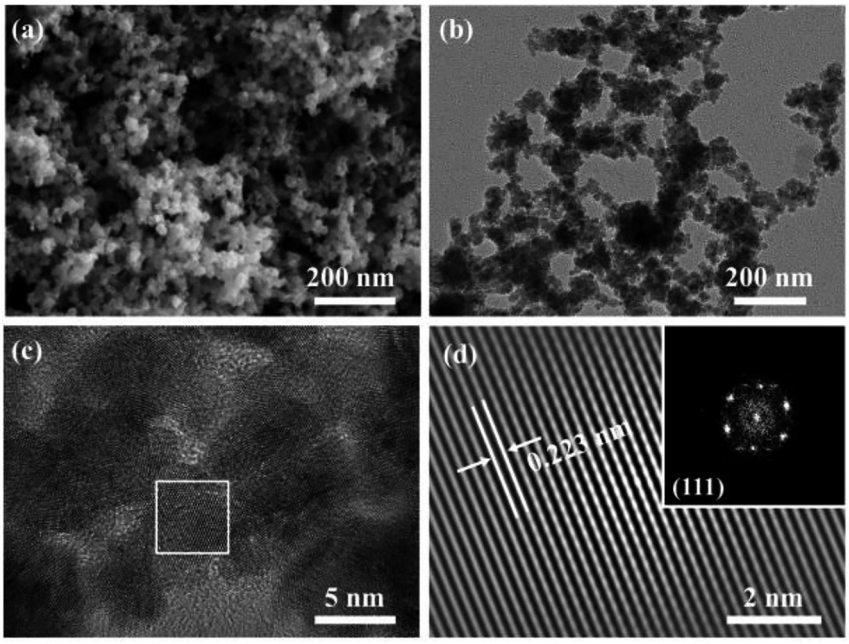

Fig. 4: (a–c). SEM, TEM, and HRTEM images of the PdRu BPNs. (d). The lattice fringes and corresponding FFT pattern of the square area in (c).
Reprinted with permission from Ref. [51]. Copyright 2019 American Chemical Society.

reported that multi-shelled hollow Cr_2O_3 microspheres (MHCMs) had a high yield rate of 25.3 μg h^{-1} mg_{cat}^{-1} and a high FE of 6.78 % for NH_3 electrosynthesis. It was higher than the corresponding Cr_2O_3 nanoparticles (13.8 μg h^{-1} mg_{cat}^{-1}, 4.73 %) and Cr_2O_3 microspheres (11.4 μg h^{-1} mg_{cat}^{-1}, 2.94 %), respectively. MHCMs showed good electrochemical and structural stability during NRR (Fig. 5). The X-ray diffraction (XRD) pattern of MHCMs (Fig. 5(a)) described the characteristic peaks of the Cr_2O_3 phase. Figure 5(b) and (c) showed the SEM images of precursor consists of microspheres with smooth surface and broken spheres with smaller size after the precursor was calcinated in air. Figure 5(d) and (e) showed the TEM images of darker periphery and lighter regions of MHCM indicating the structure of Cr_2O_3 was multishelled hollow microsphere. HRTEM image (Fig. 5(f)) revealed the lattice fringe and the interval was determined as 0.248 nm indexed to the (110) plane of Cr_2O_3 phase. Figure 5(g) described the scanning TEM (STEM) image of MHCM. As shown in Fig. 5(h) and (i), the images of Energy-dispersive X-ray (EDX) revealed that Cr and O elements were uniformly distributed on the MHCM. On the one hand, the hollow structure of the MHCMs exposed a large number of active sites and enhanced the diffusion of N_2, the intermediates and products [55]. On the other hand, the hollow structure also facilitated the frequency collisions and residence time in the inner surface. As a result, MHCMs showed preferable electrocatalytic activity for NRR.

Han et al. [56]. designed Nb_2O_5 nanofiber for N_2 fixation to NH_3 at ambient conditions. At –0.55 V vs. RHE, Nb_2O_5 nanofiber showed a high average yield rate of 43.6 μg h^{-1} mg_{cat}^{-1} compared with the NH_3 yield of commercial Nb_2O_5 (8.9 μg h^{-1} mg_{cat}^{-1}), a superior FE of 9.26 %, and outstanding electrochemical stability in 0.1 M HCl. It can be attributed to its porous surface, which exposed more active sites and enhanced the diffusion of N_2 and product.

Wu et al. [57]. synthesized Mn_3O_4 nanocube as electrocatalyst for NRR. It had a FE of 3.0 % and a NH_3 yield of 11.6 μg h^{-1} mg_{cat}^{-1} at –0.80 V vs. RHE in 0.1 M Na_2SO_4. Furthermore, this catalyst also possessed satisfactory electrochemical and structural durability. Li et al. [58] reported spinel $LiMn_2O_4$ nanofiber as electrocatalyst for NRR under ambient conditions, achieving a high NH_3 yield rate of 15.83 μg h^{-1} mg_{cat}^{-1} at –0.5 V vs. RHE in 0.1 M HCl. Meanwhile, it also showed excellent electrochemical and structure stability.

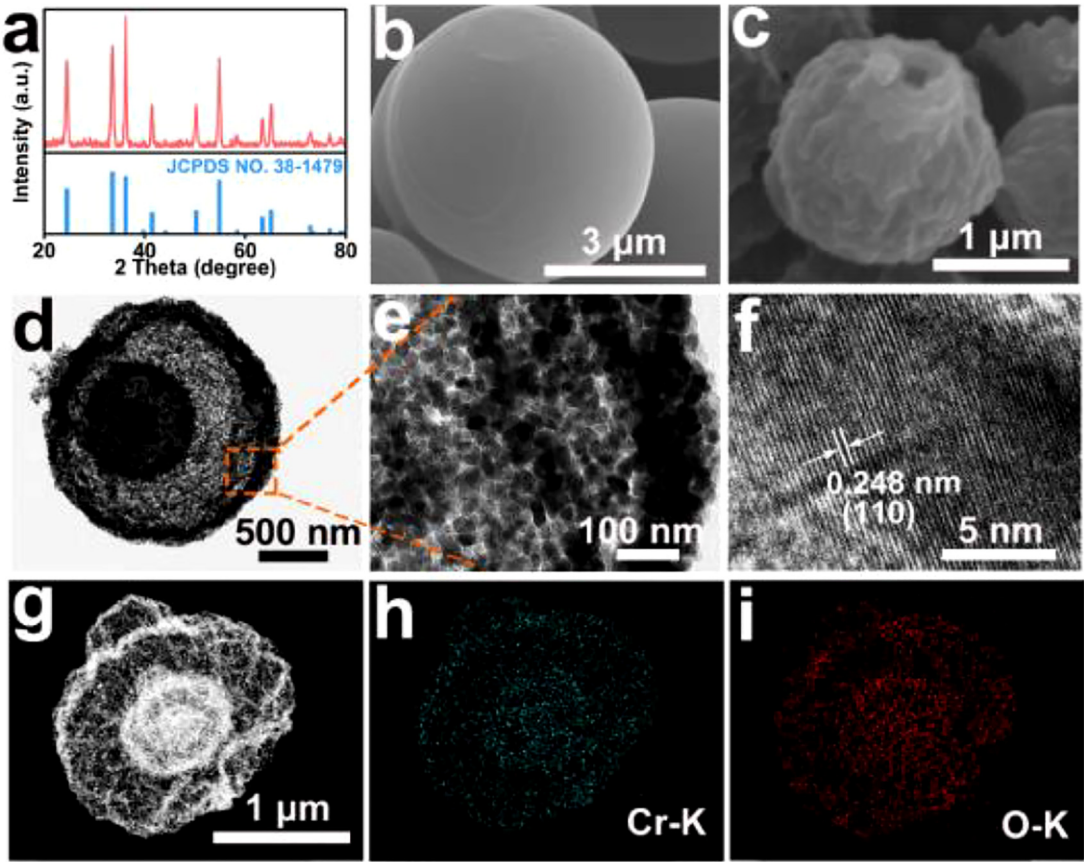

Fig. 5: (a) XRD pattern of MHCMs. SEM images of (b) the precursor of MHCMs and (c) MHCMs. (d, e) TEM images indifferent magnifications of a single MHCM. (f) HRTEM image of MHCM. (g) STEM image of MHCM and EDX elemental mapping of (h) Cr and (i) O. Reprinted with permission from Ref. [54]. Copyright 2018 American Chemical Society.

Zhao et al. [59] designed Fe nanodot-decorated MoS_2 nanosheets as an efficient electrocatalyst for N_2 fixation to NH_3 at ambient conditions. It achieved a high yield rate of 12.5 mg h^{-1} cm^{-2} and a FE of 10.8 % at −0.1 V vs. RHE. Furthermore, it showed an excellent long-term stability.

Doping and defects engineering

Doping and defects construction are common method in the design of catalysts for NRR. A large amount of efficient electrocatalysts have been designed and prepared, such as O-doped graphdiyne [60], metal-organic-framework-derived Co-doped carbon [61], Fe-doped phosphorene [62], nitrogen vacancies on 2D layered W2N3 [63], Mo-doped g-GaN monolayer [64], O-doped molybdenum carbide nanoparticles [65], nitrogen-doped NiO nanosheet [66], P-Doped graphene [67] and P-doped WO3 flowers [68].

Boron (B) is an important doping element. The B-doped graphene catalysts [69] can attain a yield rate of NH_3 formation of 9.8 μg h^{-1} cm^{-2} and a FE of 10.8 % in aqueous solutions at −0.5 V vs. RHE. The NH_3 yield and FE of B-doped was 5-fold and 10-fold higher than that of undoped graphene, respectively. The original sp2 hybridization and conjugated planar structure graphene framework doped with B atoms were retained. B doping led to electron redistribution and induced electron deficiency, resulting in a great enhancement in electrocatalytic activity. The positively charged B atom provided ideal catalytic centers for the formation of B-N bonds and subsequent production of NH_3 by facilitating the adsorption of N_2.

Qiu et al. [70] synthesized B_4C nanosheets decorated with in situ-derived B-doped graphene quantum dots for NRR. It showed a NH_3 yield rate of 28.6 μg h^{-1} mg^{-1} and a FE of 16.7 % in 0.1 M HCl under ambient conditions.

Quantum dots are important components of electrocatalysts due to their large number of exposed edge positions and unique electronic properties [71]. The B-doped graphene quantum dots exhibited large N_2 adsorption capacity and enhanced charge transfer processes, which can enhance the electrocatalytic activity for N_2-to-NH_3 conversion.

Wang et al. [72] found that B-doped TiO_2 had a highly efficient NRR performance (3.4 % at −0.8 V vs. RHE) and outstanding electrochemical durability (Fig. 6). The XRD images of pristine TiO_2 and B-TiO_2 indicated the increase of TiO_2 crystallinity as shown in Fig. 6(a). Figure 6(b) revealed the morphology of B-TiO_2 was sphere with strong agglomeration by SEM. As shown in Fig. 6(c), the EDX images revealed the uniformed distribution of Ti and O elements and low content of B was detected in the surface of particles. The TEM image revealed the sphere nature of B-TiO_2 (Fig. 6(d)). As shown in Fig. 6(e), the lattice fringe was determined as 0.35 nm indexed to the (101) plane of TiO_2 by HRTEM. And four diffraction rings indexed to the (101), (103), (200) and (211) planes of the TiO_2 phase were observed by the selected area electron diffraction (SAED). The activity was higher than pristine TiO_2 and TiO_2 nanosheets. B-TiO_2 presented higher specific surface area and exposed active sites. It can promote the electrochemical performance via the formation of oxygen vacancies. A suitable amount of B doped in TiO_2 may change the semiconductor properties of intrinsic TiO_2, which improved the conductivity of TiO_2 and contributed to electron transfer from catalyst to N_2.

Wang et al. [73] biomimetically designed a Mo(IV)-doped FeS_2 nanosheet for NRR. It showed a high NH_3 FE of 14.41 % and a yield rate of 25.15 μg h^{-1} mg^{-1} at −0.2 V vs. RHE (Fig. 7). SEM images (Fig. 7(a)) showed that the

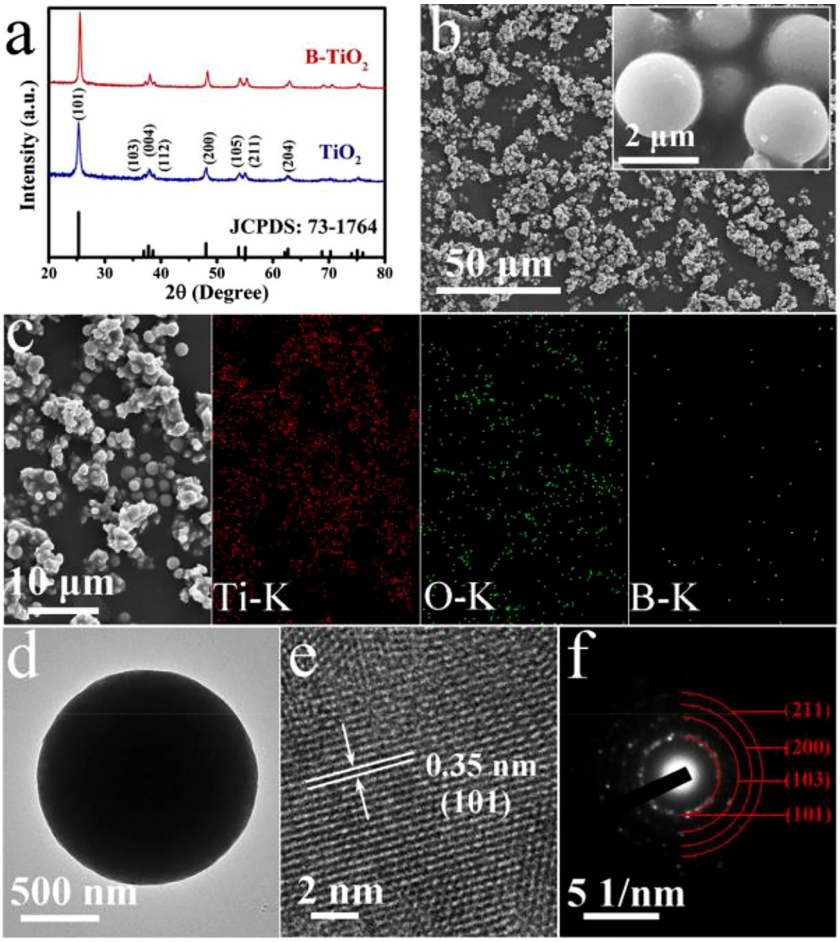

Fig. 6: (a) XRD patterns for B-TiO_2 and TiO_2. (b) SEM images of B-TiO_2. (c) SEM and EDX elemental mapping images of Ti, O and B for BTiO_2. (d) TEM image for one single B-TiO_2 particle. (e) HRTEM image and (f) SAED pattern taken from B-TiO_2.
Reprinted with permission from Ref. [72]. Copyright 2019 American Chemical Society.

catalyst was composed of thin nanosheets. Energy dispersive spectrometer (EDS) mapping revealed that the distribution of Fe, Mo, and S are homogenous (Fig. 7(b)). High-angle annular dark field scanning transmission electron microscopy (HAADF-STEM) image indicated separated bright spots assigned as Mo sites as shown in Fig. 7(c). XRD (Fig. 6(d)) images of FeS_2-Mo_x is consistent with that of pyrite FeS_2. Raman spectrum (Fig. 7(e)) of FeS_2-$Mo_{17.3}$ was almost consistent with that of FeS_2. A red shift of 10 cm^{-1} generated for the depression of Fe-S vibration by Mo doping. The valence state (+4) of Mo cations in FeS_2-$Mo_{17.3}$ was the same as those in MoS_2 according to the X-ray photoelectron spectroscopy (XPS) images (Fig. 7(f)). The adsorption and activation of N_2 was promoted by the Mo(IV) ions, and the competitive HER was depressed by the FeS_2 substrate. It has been demonstrated that Mo(IV) could be used as the active site for N_2 fixation due to its unoccupied *d* orbitals.

Li et al. [74] designed a defect-rich MoS_2 nanoflower with the high catalytic performance and strong electrochemical stability for NRR (Fig. 7). In 0.1 M Na_2SO_4, it achieved a high NH_3 yield rate of

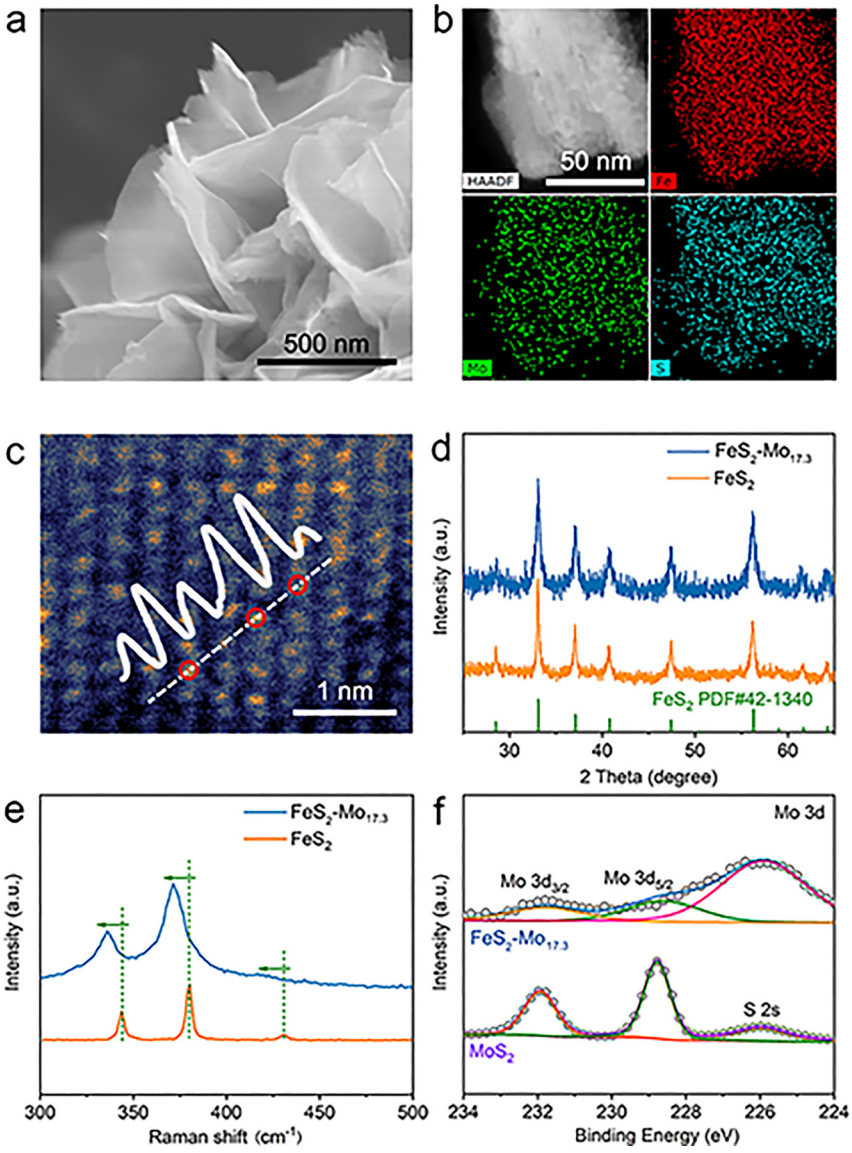

Fig. 7: Characterizations of FeS_2-$Mo_{17.3}$ nanosheets.
(a) SEM image, (b) EDS mapping, (c) HAADF-STEM image, the inset is the intensity profile of the atoms along the dot line, and the red circles indicate the Mo cations, (d) XRD patterns of FeS_2-$Mo_{17.3}$ and FeS_2 nanosheets, (e) Raman spectra of FeS_2-$Mo_{17.3}$ and FeS_2 nanosheets, and (f) Mo 3d core-level XPS spectra of FeS_2-$Mo_{17.3}$ and MoS_2. Reprinted with permission from Ref. [73]. Copyright 2020 American Chemical Society.

29.28 μg h^{-1} mg_{cat}^{-1} and a FE of 8.34 % at −0.40 V vs. RHE, superior to defect-free counterpart (13.41 μg h^{-1} mg_{cat}^{-1} and 2.18 %). It has been found that the potential determination step of the defect-rich catalyst had a lower energy barrier (0.60 eV) compared to the defect-free catalyst (0.68 eV) according to density functional theory calculations. The defects evolved the boundaries of the crystal to eliminate strain, leading to the lattice expansion. They offered more active unsaturated atoms and powerfully affected the electronic structure. For example, the defects caused the center of the d band shift to the Fermi level (−0.26 eV → −0.14 eV), resulting in boosting the interaction between the catalyst surface and N_2 molecules.

Single-atom engineering

To solve the significant challenge of N_2 fixation under ambient conditions, Tao et al. [75] studied single-atom Ru as an electrocatalyst for NRR. When ZrO_2 was used as support, a remarkably large NH_3 FE of up to 21 % can be obtained. It has been found that the addition of ZrO_2 significantly suppressed the competitive HER. The Ru sites with oxygen vacancies were the main active sites, and their high catalytic performance can be attributed to the stabilization of *NNH (low overpotential), the violent instability of *H (high NRR/HER selectivity) and N_2 adsorption enhancement (initiation of the NRR process).

Qin et al. [76] synthesized single-site Au catalysts on hierarchical N-doped porous carbon (NDPCs) for NRR. It showed a NH_3 yield rate of 2.32 μg $h^{-1}cm^{-2}$ and a FE of 12.3 % (Fig. 8).Compared with heteroatom-free porous carbon, NDPCs can stabilize the single metal sites at high loadings. This highly polarized porous carrier can be used to boost N_2 adsorption and mass transfer [77]. It has been reported that the dissociation of N_2 can be enhanced by N species in the NDPCs.

Using first-principles calculations, Tang et al. [78] reported that single transition metals (TM) atom sandwiched between hexagonal boron nitride (h-BN) and graphene sheets (BN/TM/G) acted as catalysts for NRR. TM atoms can provide electrons to adjacent B atoms as active sites. N≡N strong bond was weakened through B-to-N π-back bonding between the partially occupied *pz* orbital of a B atom and the antibonding state of N_2. The not-strong-not-weak electric field on the h-BN surface greatly enhanced the adsorption and activation of N_2. All above results provided an attractive way for triggering and modulating the activity of an inert BN sheet and created a new possibility of enhancing NH_3 production.

Fe-(O-C2)4 single-atom [79], single Mo atom supported on defective BC2N monolayers [80], single Mo atom supported on graphene [81], single-Mo-atom-embedded-graphdiyne monolayer with ultra-low onset potential [82],single Mo atom anchored on N-doped carbon [83], single-atom Pd sites with Cu [84], graphene-boron nitride hybrid-supported single Mo atom [85], single atoms of iron on MoS2 nanosheets [7], single Au/Fe atoms supported on nitrogen-doped porous carbon [86] and copper single atoms anchored in porous nitrogen-doped carbon [87] are also used as efficient for NRR under ambient conditions.

The design of nanocatalysts for NITRR

Nano-structure construction and nanoconfinement

Wang et al. [88] enhanced nitrate-to-NH_3 activity of Cu-Ni alloys through the tuning of intermediate adsorption. The electrocatalyst achieved a high FE of 99 ± 1 % in the mixture of 100 mM KNO_3 and 1 M KOH electrolyte at −0.15 V vs. RHE (Fig. 8). The $Cu_{50}Ni_{50}$ catalyst exhibited dendritic morphologies according to SEM images (Fig. 8(a)). HRTEM images of the $Cu_{50}Ni_{50}$ catalyst (Fig. 8(b)) showed that lattice spacings of 0.208 and 0.179 nm for the Cu(111) and Cu(200) facets. Fig. 8(d) described the HRTEM image of the pure Cu catalyst which exhibited the lattice spacings of 0.210 and 0.181 nm for Cu(111) and Cu(200) facets that agree with cubic Cu. As shown in Fig. 8(e)–(h), the Cu-to-Ni ratio in the $Cu_{50}Ni_{50}$ catalyst was 52:48. A decrease of Cu lattice spacings was shown when Ni was incorporated (Fig. 8(i)). XPS (Fig. 8(j)) presented a remarkable decrease of Cu 2p binding energy and an important increase of Ni 2p binding energy for the alloyed catalysts. The activity of $Cu_{50}Ni_{50}$ alloy catalysts corresponded to 6-fold increase in activity of pure Cu.

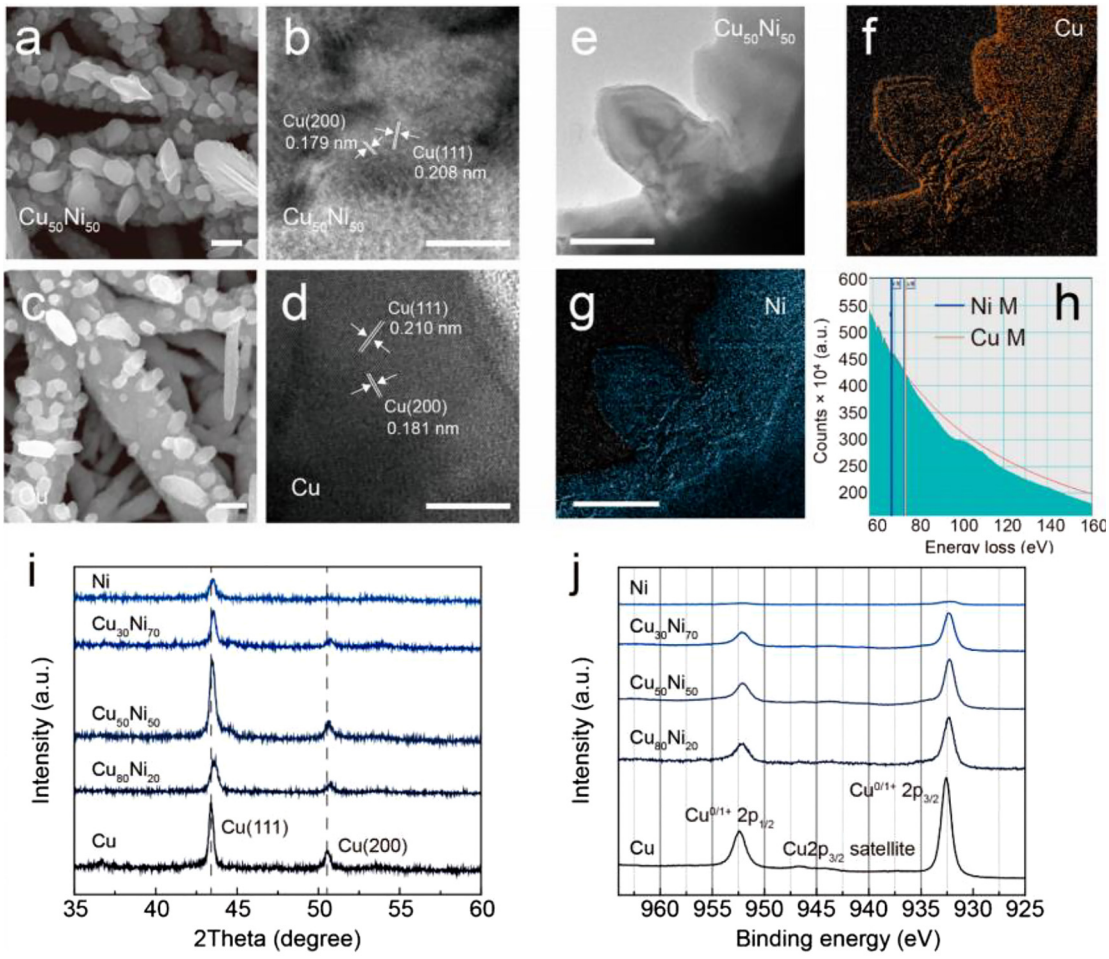

Fig. 8: Materials characterization of copper-nickel alloy catalysts.
(a, b) Representative SEM and HRTEM images of the $Cu_{50}Ni_{50}$ catalyst. (c, d) Representative SEM and HRTEM images of the pure Cu catalyst. The scale bars are 200 nm in (a) and (c), and 10 nm in (b) and (d). (e–h) STEM image and EELS mapping analysis of the $Cu_{50}Ni_{50}$ catalyst. The scale bars are 100 nm. (i, j) XRD patterns and XPS Cu 2p spectra of catalysts with different Cu:Ni ratios. Reprinted with permission from Ref. [88]. Copyright 2020 American Chemical Society.

The introduction of Ni atoms shifts the potential-dependent step (PDS) from NO_3 adsorption to NH_2 hydrogenation, reducing the overpotential.

Rai et al. [89] adopted Ni nanoparticles immobilized on Fe_3O_4@n-SiO_2@h-SiO_2-NH_2 (a magnetic hierarchical mesoporous amine-functionalized (M-HMAF) silica) support to realize efficient and selective catalytic nitrate to NH_3 at room-temperature. Notably, the Ni/M-HMAF silica possessed the capacity of superb dispersion of Ni nanoparticles over the support. The electrocatalysts exhibited a noteworthy catalytic turnover frequency of 275 mmol g^{-1} h^{-1}.

Doping and defects engineering

Jia et al. [90] reported that TiO_2 nanotubes with rich oxygen vacancies (TiO_{2-x}) can be regarded as an efficient electrocatalyst for boosting nitrate electroreduction to NH_3. It achieved a high FE of 85.0 %, a good selectivity of 87.1 % and an excellent conversion of 95.2 % at –1.6 V vs. saturated calomel electrode (SCE) (Fig. 9). The ammonium selectivity and yield of TiO_{2-x} were stable according to Fig. 9(a) and (b). Furthermore, Fig. 9(c) and (d) showed that the post-test TiO_{2-x} possessed the tubular morphology and anatase structure with

abundant oxygen vacancies. TiO_{2-x} had tubular morphology and anatase structure with abundant oxygen vacancies (OVs). OVs weakened the N–O bond and inhibited the formation of by-products, which resulted in excellent selectivity.

Li et al. [91] designed Ru/O-doped-Ru core/shell nanoclusters as efficient NH_3 electrosynthesis catalysts from nitrate. The electrocatalyst showed a high NH_3 yield rate of 5.56 mol g_{cat}^{-1} h^{-1}, which was obviously higher than that of Haber-Bosch process. The strained Ru nanoclusters were equipped with the characteristic of building a firm bonding between the Ru and subsurface O dopants. The O dopants can trigger tensile strains by expanding Ru unit cell. The strain unit cells inhibited HER. However, the strains facilitated the barrier of H–H coupling to promote the formation of •H. Hydrogen radicals are major contributors to this high catalytic performance, enhancing the hydrogenation of reaction intermediates to NH_3 at lower kinetic barriers. As a result of stable subsurface Ru-O coordination, it was possible for the strained nanostructures to maintain nearly 100 % ammonia-evolving selectivity at >120 mA cm^{-2} current densities for 100 h.

Single-atom engineering

Feng et al. [92] reported that atomic Cu anchored on carbon nanosheets showed excellent stability and activity for NITRR. Compared with nanoparticles and bulk materials, Cu single atom exhibited higher adsorption ability of NO_3^- and NO_2^-.

Niu et al. [93] took graphite carbon nitride (g-CN) supported single transition metal atoms as an example and demonstrated the NITRR feasibility of single atom catalyst (SACs) by DFT calculation. Represented by a single transition metal atom catalyst (from Ti to Au) supported by g-CN, the NITRR performance of SACs was studied comprehensively by first principle calculation. The mechanism of transforming NO_3^- into NH_3 was summed up as an O-end, O-side, N-end, N-side, and NO-dimer approach. Volcano and contour plots were established to explain the activity trends on the catalysts. The results showed that the high efficiency of NITRR was realized on Ti/g-CN and Zr/g-CN, and the limit potentials were −0.39 and −0.41, respectively. This work provided a way for the application of SACs and lays a foundation for the development of NITRR.

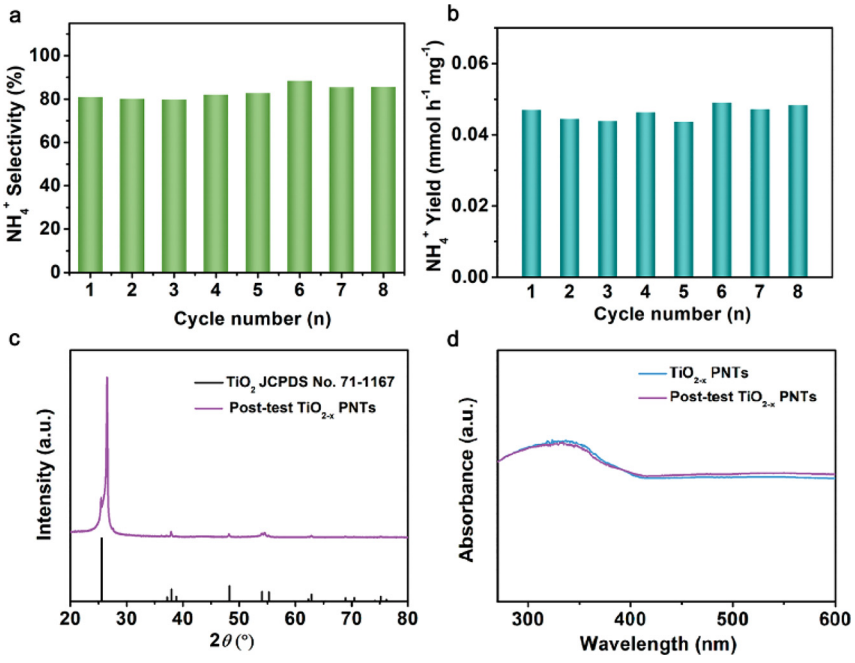

Fig. 9: (a) Selectivity and (b) yield rate of ammonium after consecutive recycling test. (c) XRD pattern of post-test TiO_{2-x}. (d) UV–vis absorption spectra of TiO_{2-x} and post-test TiO_{2-x}. Reprinted with permission from Ref. [90]. Copyright 2020 American Chemical Society.

Summary and perspectives

NH_3 electrosynthesis is attractive and important because of its high energy efficiency and non-polluting characteristics. The continuous progress has been made and feasibility of nanocatalysts for the reaction under ambient conditions has been demonstrated. In this review, we have introduced a number of electrocatalysts in NRR (Table 1) and NITRR (Table 2) with a high NH_3 yield rate and FE from three aspects, including nano-structure construction/nanoconfinement, doping/defects engineering and single-atom engineering. Nano-structure construction and nanoconfinement effects change the motion characteristics of electrons, leading to the change of electronic structure and higher activity and selectivity, especially for the valence electron structure. Doping promotes the occurrence of catalytic reactions by promoting charge transfer and the electrical conductivity. Defect plays an important role in electrocatalysts to regulate the properties of the surfaces/interfaces. Both of them provide higher active and selective sites, and reduce the apparent activation energy. Single-atom catalysts with atomically dispersed metal active sites, are well used in overcoming the limitations of nanoparticles and bulk materials during the catalytic process.

Despite the remarkable achievements made in the field, many challenges are still required to be overcome for ambient NH_3 electrosynthesis via NRR or NITRR.

Further improving the selectivity and yield of NH_3

It is worth noting that the unsatisfactory conversion efficiency still remains as a great challenge, including a low NH_3 yield rate, and limited Faradaic efficiency. Therefore, various highly efficient electrocatalytic systems need to be explored to promote the development of N_2 or NO_3^- conversion technology, including electrocatalysts, electrolytes, and electrochemical cells. New design strategies will be developed to boost the activity of the catalysts, such as construction of multiple functional sites, optimizing metal-support interface, catalyst-electrolyte interface engineering and so on [94]. Briefly, the multiple active sites should exhibit a favorable spatial arrangement to enable the mutual interaction between distinct intermediates. Constructing multiple active sites in catalyst is important for the multistep synthesis of chemicals via tandem electrocatalytic reactions. The strong metal-support interaction will induce electronic modification on the supported metals, impact adsorption behaviors, and affect the catalytic activity and selectivity. Finally, the interactions at the interface of catalyst-electrolyte can also regulate the diffusion of proton donors, enrich the local concentration of reactant molecules, and tune the intermediate binding strength, influencing the catalytic performance.

Besides, several research actions can be also applied to enhance the performance of NRR and NITRR, such as applying magneto-electrochemistry and modifying 3D electrode architectures [95], interfacial polarization triggered by single-atom protrusions [96].

Applying operando characterization techniques

Up to now, many ex situ characterization techniques have been utilized to gain insight into the composition, morphology and structure of the electrocatalysts. However, the operando characterizations require to be carried out to probe the change of the active sites, such as the oxidation state, the geometric and electronic structure, the electrode/electrolyte interface, etc. Various operando characterization techniques have received much attention in the past decades, including operando XRD, operando X-ray absorption (XAS), operando XPS, operando Raman and infrared radiation (IR) spectroscopy and operando microscopy. Through the combination of experimental observations and theoretical calculations, we can get the deep insight into the knowledge of the active site structures, the reaction pathways, and the possible mechanisms. Furthermore, the understanding of the structure-activity relationship also provides a guideline for the rational design of catalysts.

Table 1: Comparison of the electrocatalytic NRR performance under ambient conditions.

	Catalyst	Synthesis method	Electrolyte	Potential (V vs. RHE)	FE	v_{NH3}	Stability (h)	Ref.
Nano-structure construction/ nanoconfinement	CoMoC nanoporous	Electrochemical dealloying method	0.1 M PBS (PH = 7)	0.1	8.9 %	18.9 μg cm^{-2} h^{-1}	24 h	[26]
	$FeMo_3S_4$ nanorods	Hydrothermal approach	0.5 M $LiClO_4$	−0.3	19.2 %	65.3 μg h^{-1} mg^{-1}	20 h	[27]
	FeMoO4 nanorods	Solvothermal method	0.1 M Na_2SO_4	−0.6	10.53 %	17.51 μg h^{-1} mg^{-1}	12 h	[28]
	CrN nanocube	Hydrothermal method	0.1 M HCl	−0.5	16.6 %	31.11 μg h^{-1} mg^{-1}	2 h	[29]
	$Fe_2(MoO_4)_3$ nanoparticles	Wet chemical methods	0.1 M Na_2SO_4	−0.6	9.1 %	18.16 μg h^{-1} mg^{-1}	24 h	[30]
	Three-dimensional Pd-Ag-S porous nanosponges	Two-step process	0.1 M Na_2SO_4	−0.2	18.41 %	9.73 μg h^{-1} mg^{-1}	20 h	[32]
	MoO2 nanoparticles supported by carbon nanowires		0.1 M HCl	−0.1	30 %	21.2 μg h^{-1} mg^{-1}	12 h	[34]
	Au nanocrystals	Wet chemical methods	1.0 M KOH	−0.2	10.2 %	20 μg h^{-1} mg^{-2}	3 h	[35]
	Ag_2O-Au-719 nanocages	Galvanic replacement techniques	0.5 M $LiClO_4$	−0.4	23.4 %	2.14 μg cm^{-2} h^{-1}		[36]
	Amorphous $CoMoO_4$ catalysts with nanoporous structures	Dealloying method	0.1 M phosphate buffer saline	−0.50	3.8 %	30.2 μg h^{-1} mg^{-1}	24 h	[39]
	Palladium nanothorn assembly array	Micelle-assisted self-reduction method	0.1 M Na_2SO_4	−0.15	20.01 %	5.45 μg h^{-1} cm^{-2}	20 h	[40]
	VN nanowire	Nitridation of V_2O_5 nanowire array precursor	0.1 M HCl	−0.3	3.58 %	2.48 × 10-10 mol^{-1} s^{-1} cm^{-2}	3 h	[41]
	Hollow Au nanocages	Galvanic replacement technique	0.5 M $LiClO_4$	−0.4	30.2 %	3.9 μg cm^{-2} h^{-1}	12 h	[43]
	Dendritic Cu	Galvanic replacement technique	0.1 M HCl	−0.4	15.12 %	25.63 μg mg^{-1} h^{-1}	24 h	[44]
	Donor–acceptor couples of Ni and Au nanoparticles	Galvanic replacement technique	0.05 M H_2SO_4	−0.14	67.8 %	7.4 μg h^{-1} mg^{-1}	2 h	[47]
	PdRu porous nanostructures	One-step $NaBH_4$ reduction	0.1 M HCl	−0.1	1.53 %	25.92 μg mg^{-1} h^{-1}	2 h	[51]
	$Pd_{0.2}Cu_{0.8}$/rGO composites	Tannic acid (TA) and $NaBH_4$ mixed reductants	0.1 M KOH	−0.2		2.8 μg h^{-1} mg^{-1}	≈1.94 h	[52]
	Nanoporous palladium hydride	Chemical dealloying	0.1 M HCl	−0.2	43.6 %	20.4 μg mg^{-1} h^{-1}	2 h	[53]
	Multi-shelled hollow Cr_2O_3 microspheres	Calcination	0.1 M Na_2SO_4	−0.9	6.78 %	25.3 μg h^{-1} mg_{cat}^{-1}	2 h	[54]
	Nb_2O_5 nanofiber	Electrospinning followed by air annealing.	0.1 M HCl	−0.55	9.26 %	43.6 μg h^{-1} mg_{cat}^{-1}	27 h	[56]

Table 1: (continued)

	Catalyst	Synthesis method	Electrolyte	Potential (V vs. RHE)	FE	v_{NH3}	Stability (h)	Ref.
	Mn_3O_4 nanocube	Hydrothermal method	0.1 M Na_2SO_4	−0.50	3.0 %	11.6 μg h^{-1} mg_{cat}^{-1}	24 h	[57]
	Spinel $LiMn_2O_4$ nanofiber	Electrospinning followed by air annealing	0.1 M HCl	−0.5	7.44 %	15.83 μg h^{-1} mg_{cat}^{-1}	24 h	[58]
	Fe nanodot-decorated MoS_2 nanosheets	Hydrothermal reaction and chemical reductive growth	0.1 M KOH	−0.1	10.8 %	12.5 mg h^{-1} cm^{-2}	48 h	[59]
Doping and defects engineering	Metal-organic-framework-derived Co-doped carbon	Heat-treating	0.1 M KOH	−0.3	11.53 %	4.66 μmol cm^{-2} h^{-1}	24 h	[61]
	Nitrogen vacancies on 2D layered W2N3	Annealing	0.1 M KOH	−0.2	11.67 ± 0.93 %	11.66 ± 0.98 μg h^{-1} mg_{cat}^{-1}	24 h	[63]
	O-doped molybdenum carbide nanoparticles		0.1 mM HCl + 0.5 M Li_2SO_4	−0.35	25.1 %	22.5 μg h^{-1} mg_{cat}^{-1}	30 h	[65]
	Nitrogen-doped NiO nanosheet		0.1 M $LiClO_4$	−0.5	7.3 %	22.7 μg h^{-1} mg^{-1}	12 h	[66]
	P-doped graphene	Modified Hummers method	0.5 M $LiClO_4$	−0.65	20.82 %	32.33 μg $h^{-1}mg_{cat}^{-1}$	13 h	[67]
	P-doped WO_3 flowers	Hydrothermal synthesis	0.1 M Na_2SO_4	−0.55	17.5 %	6.54 × 10−10 mol s^{-1} cm^{-2}	12 h	[68]
	B-doped graphene	Thermal reduction	0.05 M H_2SO_4	−0.5	10.8 %	9.8 μg h^{-1} cm^{-2}	10 h	[69]
	B_4C-BGQDs/CPE	*in situ* formation	0.1 M HCl	−0.45	16.7 %	28.6 μg h^{-1} mg^{-1}	20 h	[70]
	B-doped TiO_2	Calcine	0.1 M Na_2SO_4	−0.8	3.4 %	14.4 μg h^{-1} mg^{-1}	24 h	[72]
	Mo(IV)-doped FeS_2 nanosheet	Low-temperature solution-phase reaction and Solvothermal treatment	0.1 M KOH	−0.2	14.41 %	25.15 μg h^{-1} mg^{-1}	≈2.78 h	[73]
	Defect-rich MoS_2 nanoflower	Hydrothermal method	0.1 M Na_2SO_4	−0.4	8.34 %	29.28 μg h^{-1} mg^{-1}	20 h	[74]
Single-atom engineering	Ru single-atom catalysts	Pyrolyzing	0.05 m H_2SO_4	−0.2	29.6 %	120.9 μg h^{-1} mg^{-1}	12 h	[49]
	Single-atom Ru sites supported on N-doped porous carbon	Hydrothermal method	0.1 M HCl	−0.21	2 1 %	3.665 mg_{NH3} h^{-1} mg^{-1}	60 h	[75]
	N-doped porous carbon	Template-assisted method	0.1 M HCl	−0.2	12.3 %	2.32 μg h^{-1} cm^{-2}	50000s	[76]
	Fe-(O-C2)4 single-atom		0.1 M KOH	−0.1	29.3 %	32.1 mg h^{-1} $mg_{cat.}^{-1}$	40 h	[79]
	Single Mo atom anchored on N-doped carbon	Dissolution-and-carbonization method	0.05 M H_2SO_4	−0.45	24.8 ± 0.8 %	69.2 ± 2.5 μg h^{-1} $mg_{cat.}^{-1}$	30 h	[84]
	Single atoms of iron on MoS2 nanosheets	Injecting	0.5 M K_2SO_4	−0.3	18.8 %	8.63 mg_{NH3} $mg_{cat.}^{-1}$ h^{-1}		[7]
	Copper single atoms anchored in porous nitrogen-doped carbon	Surfactant-assisted synthesis approach	0.1 M KOH 0.1 M HCl		13.8 % 11.7 %	53.3 μg h^{-1} $mg_{cat.}^{-1}$ 49.3 μg h^{-1} $mg_{cat.}^{-1}$	12 h	[87]

Table 2: Comparison of the electrocatalytic NITRR performance under ambient conditions.

	Catalyst	Synthesis method	Electrolyte	Potential (V vs. RHE)	FE	v_{NH3}	Stability (h)	Ref.
Nano-structure construction/ nanoconfinement	$Cu_{50}Ni_{50}$	Electrodeposit	The mixture of 100 mM KNO_3 and 1 M KOH	−0.2	99 ± 1 %		12 h	[88]
Doping and defects engineering	TiO_2 nanotubes with rich oxygen vacancies	Calcine	0.5 M Na_2SO_4 solution	−1.6 V vs. SCE	85.0 %	0.045 mmol h^{-1} mg^{-1}	2 h	[90]
	Ru/O-doped-Ru core/shell nanoclusters	Sol-gel route and cyclic voltammetry	Mixture of 1 M KOH and 1 M KNO_3			5.56 mol g_{cat}^{-1} h^{-1}	100 h	[91]
Single-atom engineering	Single-atom Cu	Pyrolysis		−1.3			24 h	[92]

Developing new reaction routes based on NRR and NITRR

Using electrochemical method to synthesize organic molecules possesses various advantages, such as mild conditions, high functional group tolerance, and innate scalability and sustainability. By coupling NRR or NITRR, some thermodynamically unfavorable reactions have been successfully achieved, such as the production of urea under ambient conditions. It can be expected that this methodology is promising to develop new reaction routes that is difficult or even impossible under normal condition.

Research funding: This work was supported by the National Key Research and Development Program of China (2017YFA0403101), National Natural Science Foundation of China (22002172, 21733011), and the Chinese Academy of Sciences (QYZDY-SSWSLH013).

References

[1] R. Schlogl. *Angew. Chem. Int. Ed.* **42**, 2004 (2003).
[2] J. Kong, A. Lim, C. Yoon, J. H. Jang, H. C. Ham, J. Han, S. Nam, D. Kim, Y.-E. Sung, J. Choi, H. S. Park. *ACS Sustain. Chem. Eng.* **5**, 10986 (2017).
[3] L. Wang, M. Xia, H. Wang, K. Huang, C. Qian, C. T. Maravelias, G. A. Ozin. *Joule* **2**, 1055 (2018).
[4] Y. H. Lu, Y. Yang, T. F. Zhang, Z. Ge, H. Chang, P. Xiao, Y. Xie, L. Hua, Q. Li, H. Li, B. Ma, N. Guan, Y. Ma, Y. Chen. *ACS Nano* **10**, 10507 (2016).
[5] M. D. Fryzuk, J. B. Love, S. J. Rettig, V. G. Young. *Science* **275**, 1445 (1997).
[6] J. D. Benck, T. R. Hellstern, J. Kibsgaard, P. Chakthranont, T. F. Jaramillo. *ACS Catal.* **4**, 3957 (2014).
[7] H. Su, L. Chen, Y. Chen, R. Si, Y. Wu, X. Wu, Z. Geng, W. Zhang, J. Zeng. *Angew. Chem. Int. Ed.* **59**, 20411 (2020).
[8] Z. Li, S. Ji, Y. Liu, X. Cao, S. Tian, Y. Chen, Z. Niu, Y. Li. *Chem. Rev.* **120**, 623 (2020).
[9] X. Sun, L. Lu, Q. Zhu, C. Wu, D. Yang, C. Chen, B. Han. *Angew. Chem. Int. Ed.* **57**, 2427 (2018).
[10] Y. Wu, S. Cao, J. Hou, B. Zhang, P. Zhai, Y. Zhang, L. Sun. *Adv. Energy Mater.* **10**, 2000588 (2020).
[11] Y. Zhou, F. Che, M. Liu, C. Zou, Z. Liang, P. D. Luna, H. Yuan, J. Li, Z. Wang, H. Xie, H. Li, P. Chen, E. Bladt, R. Quintero-Bermudez, T. K. Sham, S. Bals, J. Hofkens, D. Sinton, G. Chen, E. H. Sargent. *Nat. Chem.* **10**, 974 (2018).
[12] Q. Wang, Y. Lei, D. Wang, Y. Li. *Energy Environ. Sci.* **12**, 1730 (2019).
[13] M. Li, H. Wang, W. Luo, P. C. Sherrell, J. Chen, J. Yang. *Adv. Mater.* **32**, 2001848 (2020).
[14] Y. Chen, R. Gao, S. Ji, H. Li, K. Tang, P. Jiang, H. Hu, Z. Zhang, H. Hao, Q. Qu, X. Liang, W. Chen, J. Dong, D. Wang, Y. Li. *Angew. Chem. Int. Ed.* **60**, 3212 (2020).
[15] L. Zhang, Y. Ren, W. Liu, A. Wang, T. Zhang. *Natl. Sci. Rev.* **5**, 653 (2018).
[16] H. Shang, X. Zhou, J. Dong, A. Li, X. Zhao, Q. Liu, Y. Lin, J. Pei, Z. Li, Z. Jiang, D. Zhou, L. Zheng, Y. Wang, J. Zhou, Z. Yang, R. Cao, R. Sarangi, T. Sun, X. Yang, X. Zheng, W. Yan, Z. Zhuang, J. Li, W. Chen, D. Wang, J. Zhang, Y. Li. *Nat. Commun.* **11**, 3049 (2020).
[17] X. Sun, C. Chen, S. Liu, S. Hong, Q. Zhu, Q. Qian, B. Han, J. Zhang, L. Zheng. *Angew. Chem. Int. Ed.* **58**, 4669 (2019).
[18] M. Shreya, A. C. David, K. Stavros, K. Liu, H. Zhang, S. Zhao, H. Xu, K. L. More, G. Wang, G. Wu. *Nanomater. Energy* **48**, 217 (2018).
[19] J. Martínez, A. Ortiz, I. Ortiz. *Appl. Catal, B* **207**, 42 (2017).
[20] A. Das, A. S. Nair, B. Pathak. *J. Phys. Chem. C* **124**, 20193 (2020).
[21] J. X. Liu, D. Richards, N. Singh, B. R. Goldsmith. *ACS Catal.* **9**, 7052 (2019).
[22] J. Choi, B. H. R. Suryanto, D. Wang, H.-L. Du, R. Y. Hodgetts, F. M. Ferrero Vallana, D. R. MacFarlane, A. N. Simonov. *Nat. Commun.* **11**, 5546 (2020).
[23] S. Z. Andersen, V. Čolić, S. Yang, J. A. Schwalbe, A. C. Nielander, J. M. McEnaney, K. Enemark-Rasmussen, J. G. Baker, A. R. Singh, B. A. Rohr, M. J. Statt, S. J. Blair, S. Mezzavilla, J. Kibsgaard, P. C. K. Vesborg, M. Cargnello, S. F. Bent, T. F. Jaramillo, I. E. L. Stephens, J. K. Nørskov, I. Chorkendorff. *Nature* **570**, 504 (2019).
[24] L. Li, C. Tang, D. Yao, Y. Zheng, S.-Z. Qiao. *ACS Energy Lett.* **4**, 2111 (2019).
[25] Y. Zhao, R. Shi, X. Bian, C. Zhou, Y. Zhao, S. Zhang, F. Wu, G. I. N. Waterhouse, L. Z. Wu, C. H. Tung, T. Zhang. *Adv. Sci.* **6**, 1802109 (2019).
[26] L. Xiao, Z. Cui, S. Zhu, Y. Liang, Z. Li, S. Wu, C. Chang, S. Luo. *Appl. Surf. Sci.* **521**, 146385 (2020).
[27] J. Wang, H. Nan, Y. Tian, K. Chu. *ACS Sustain. Chem. Eng.* **8**, 12733 (2020).
[28] J. Wu, Z. Wang, S. Li, S. Niu, Y. Zhang, J. Hu, J. Zhao, P. Xu. *Chem. Commun.* **56**, 6834 (2020).
[29] Z. Ma, J. Chen, D. Luo, T. Thersleff, R. Dronskowski, A. Slabon. *Nanoscale* **12**, 19276 (2020).
[30] H. Xian, H. Guo, Z. Chen, G. Yu, A. A. Alshehri, K. A. Alzahrani, F. Hao, R. Song, T. Li. *ACS Appl. Mater. Interfaces* **12**, 2445 (2020).
[31] Q. Li, L. He, C. Sun, X. Zhang. *J. Phys. Chem. C* **121**, 27563 (2017).

[32] H. Wang, S. Liu, H. Zhang, S. Yin, Y. Xu, X. Li, Z. Wang, L. Wang. *Nanoscale* **12**, 13507 (2020).
[33] L. Yu, J. Qin, W. Zhao, Z. Zhang, J. Ke, B. Liu. *Int. J. Photoenergy* **2020**, 5251431 (2020).
[34] X. Han, C. S. Gerke, S. Banerjee, M. Zubair, J. Jiang, N. M. Bedford, E. M. Miller, V. S. Thoi. *ACS Energy Lett.* **5**, 3237 (2020).
[35] W. Zhang, Y. Shen, F. Pang, D. Quek, W. Niu, W. Wang, P. Chen. *ACS Appl. Mater. Interfaces* **12**, 41613 (2020).
[36] M. Nazemi, M. A. El-Sayed. *J. Phys. Chem. C* **123**, 11422 (2019).
[37] X. Wu, Z. Wang, Y. Han, D. Zhang, M. Wang, H. Li, H. Zhao, Y. Pan, J. Lai, L. Wang. *J. Mater. Chem. A.* **8**, 543 (2019).
[38] H. Wang, D. Yang, S. Liu, S. Yin, Y. Xu, X. Li, Z. Wang, L. Wang. *ACS Sustain. Chem. Eng.* **7**, 15772 (2019).
[39] L. Xiao, Y. Liang, Z. Li, S. Wu, S. Zhu, S. Luo, C. Chang, Z. Cui. *ACS Sustain. Chem. Eng.* **8**, 19072 (2020).
[40] S. Liu, Z. Wang, H. Zhang, S. Wang, P. Wang, Y. Xu, X. Li, L. Wang, H. Wang. *ACS Sustain. Chem. Eng.* **8**, 14228 (2020).
[41] X. Zhang, R. M. Kong, H. Du, L. Xia, F. Qu. *Chem. Commun.* **54**, 5323 (2018).
[42] G. Liu, C. Zhao, S. Ding. *New J. Chem.* **44**, 21070 (2020).
[43] M. Nazemia, S. R. Panikkanvalappila, M. A. El-Sayeda. *Nanomater. Energy* **49**, 316 (2018).
[44] C. B. Li, S. Y. Mou, X. J. Zhu, F. Wang, Y. Wang, Y. Qiao, X. Shi, Y. Luo, B. Zheng, Q. Li, X. Sun. *Chem. Commun.* **55**, 14474 (2019).
[45] Y. Song, D. Johnson, R. Peng, D. K. Hensley, P. V. Bonnesen, L. Liang, J. Huang, F. Yang, F. Zhang, R. Qiao, A. P. Baddorf, T. J. Tschaplinski, N. L. Engle, M. C. Hatzell, Z. Wu, D. A. Cullen, H. M. Meyer, B. G. Sumpter, A. J. Rondinone. *Sci. Adv.* **4**, e1700336 (2018).
[46] M. Liu, Y. Pang, B. Zhang, P. De Luna, O. Voznyy, J. Xu, X. Zheng, C. T. Dinh, F. Fan, C. Cao, F. P. G. de Arquer, T. S. Safaei, A. Mepham, A. Klinkova, E. Kumacheva, T. Filleter, D. Sinton, S. O. Kelley, E. H. Sargent. *Nature* **537**, 382 (2016).
[47] Z. H. Xue, S. N. Zhang, Y. X. Lin, H. Su, G.-Y. Zhai, J.-T. Han, Q.-Y. Yu, X.-H. Li, M. Antonietti, J.-S. Chen. *J. Am. Chem. Soc.* **141**, 14976 (2019).
[48] H. K. Lee, C. S. L. Koh, Y. H. Lee, C. Liu, I. Y. Phang, X. Han, C.-K. Tsung, X. Y. Ling. *Sci. Adv.* **4**, eaar3208 (2018).
[49] Z. Geng, Y. Liu, X. Kong, P. Li, K. Li, Z. Liu, J. Du, M. Shu, R. Si, J. Zeng. *Adv. Mater.* **30**, 1803498 (2018).
[50] J. Wang, L. Yu, L. Hu, G. Chen, H. Xin, X. Feng. *Nat. Commun.* **9**, 1795 (2018).
[51] Z. Q. Wang, C. J. Li, K. Deng, Y. Xu, H. Xue, X. Li, L. Wang, H. Wang. *ACS Sustain. Chem. Eng.* **7**, 2400 (2019).
[52] M. M. Shi, D. Bao, S. J. Li, B.-R. Wulan, J.-M. Yan, Q. Jiang. *Adv. Energy Mater.* **8**, 1800124 (2018).
[53] W. Xu, G. Fan, J. Chen, J. Li, L. Zhang, S. Zhu, X. Su, F. Cheng, J. Chen. *Angew. Chem. Int. Ed.* **59**, 3511 (2019).
[54] Y. Zhang, W. B. Qiu, Y. J. Ma, Y. Luo, Z. Tian, G. Cui, F. Xie, L. Chen, T. Li, X. Sun. *ACS Catal.* **8**, 8540 (2018).
[55] Y. Liang, Y. Li, H. Wang, J. Zhou, J. Wang, T. Regier, H. Dai. *Nat. Mater.* **10**, 780 (2011).
[56] J. R. Hana, Z. C. Liuc, Y. J. Mad. *Nanomater. Energy* **52**, 264 (2018).
[57] X. F. Wu, L. Xia, Y. Wang, W. Lu, Q. Liu, X. Shi, X. Sun. *Small* **14**, 1803111 (2018).
[58] C. B. Li, J. L. Yu, L. Yang, J. Zhao, W. Kong, T. Wang, A. M. Asiri, Q. Li, X. Sun. *Inorg. Chem.* **58**, 9597 (2019).
[59] X. Zhao, X. Zhang, Z. Xue, W. Chen, Z. Zhou, T. Mu. *J. Mater. Chem. A.* **7**, 27417 (2019).
[60] Z. Feng, Y. Tang, W. Chen, D. Wei, Y. Ma, X. Dai. *Mol. Catal.* **483**, 110705 (2020).
[61] A. Liu, X. Liang, Q. Yang, X. Ren, M. Gao, Y. Yang, T. Ma. *ChemElectroChem* **7**, 4900 (2020).
[62] Z. Wei, Y. Zhang, S. Wang, C. Wang, J. Ma. *J. Mater. Chem. A.* **6**, 13790 (2018).
[63] H. Jin, L. Li, X. Liu, C. Tang, W. Xu, S. Chen, L. Song, Y. Zheng, S. Z. Qiao. *Adv. Mater.* **31**, 1902709 (2019).
[64] L. Li, J. M. P. Martirez, E. A. Carter. *ACS Catal.* **10**, 12841 (2020).
[65] X. Qu, L. Shen, Y. Mao, J. Lin, Y. Li, G. Li, Y. Zhang, Y. Jiang, S. Sun. *ACS Appl. Mater. Interfaces* **11**, 31869 (2019).
[66] X. Wang, J. Wang, Y. Li, K. Chu. *ChemCatChem* **11**, 4529 (2019).
[67] T. Wu, X. Li, X. Zhu, S. Mou, Y. Luo, X. Shi, A. M. Asiri, Y. Zhang, B. Zheng, H. Zhao, X. Sun. *Chem. Commun.* **56**, 1831 (2020).
[68] Y. Wang, J. Dai, M. Zhang, Y.-T. Liu, J. Yu, B. Ding. *Chem. Commun.* **56**, 12937 (2020).
[69] X. M. Yu, P. Han, Z. X. We, L. Huang, Z. Gu, S. Peng, J. Ma, G. Zheng. *Joule* **2**, 1610 (2018).
[70] W. B. Qiu, Y. X. Luo, R. P. Liang, J.-D. Qiu, X.-H. Xia. *Chem. Commun.* **55**, 7406 (2019).
[71] C. W. Lee, J. S. Hong, K. D. Yang, K. Jin, J. H. Lee, H.-Y. Ahn, H. Seo, N.-E. Sung, K. T. Nam. *ACS Catal.* **8**, 931 (2018).
[72] Y. Wang, K. Jia, Q. Pan, Y. Xu, Q. Liu, G. Cui, X. Guo, X. Sun. *ACS Sustain. Chem. Eng.* **7**, 117 (2019).
[73] H. Wang, J. Wang, R. Zhang, C.-Q. Cheng, K.-W. Qiu, Y.-j. Yang, J. Mao, H. Liu, M. Du, C.-K. Dong, X.-W. Du. *ACS Catal.* **10**, 4914 (2020).
[74] X. H. Li, T. S. Li, Y. J. Ma, Q. Wei, W. Qiu, H. Guo, X. Shi, P. Zhang, A. M. Asiri, L. Chen, B. Tang, X. Sun. *Adv. Energy Mater.* **8**, 1801357 (2018).
[75] H. Tao, C. Choi, L. Ding, Z. Jiang, Z. Han, M. Jia, Q. Fan, Y. Gao, H. Wang, A. Robertson, S. Hong, Y. Jung, S. Liu, Z. Sun. *Chem* **5**, 204 (2018).
[76] Q. Qin, T. Heil, M. Antonietti, M. Oschatz. *Small Methods* **2**, 1800202 (2018).
[77] L. Qie, W. M. Chen, Z. H. Wang, Q.-G. Shao, X. Li, L.-X. Yuan, X.-L. Hu, W.-X. Zhang, Y.-H. Huang. *Adv. Mater.* **24**, 2047 (2012).
[78] S. B. Tang, Q. Dang, T. Y. Liu, S. Zhang, Z. Zhou, X. Li, X. Wang, E. Sharman, Y. Luo, J. Jiang. *J. Am. Chem. Soc.* **142**, 19308 (2020).
[79] S. Zhang, M. Jin, T. Shi, M. Han, Q. Sun, Y. Lin, Z. Ding, L. R. Zheng, G. Wang, Y. Zhang, H. Zhang, H. Zhao. *Angew. Chem. Int. Ed.* **59**, 13423 (2020).
[80] L. Chen, Q. Wang, H. Gong, M. Xue. *Appl. Surf. Sci.* **546**, 149131 (2021).
[81] H. Y. Zhou, J. C. Li, Z. Wen, Q. Jiang. *Phys. Chem. Chem. Phys.* **21**, 14583 (2019).
[82] X. Zhai, H. Yan, G. Ge, J. Yang, F. Chen, X. Liu, D. Yang, L. Li, J. Zhang. *Appl. Surf. Sci.* **506**, 144941 (2019).

[83] C. Ling, X. Bai, Y. Ouyang, A. Du, J. Wang. *J. Phys. Chem. C* **122**, 16842 (2018).
[84] L. Han, Z. Ren, P. Ou, H. Cheng, N. Rui, L. Lin, X. Liu, L. Zhuo, J. Song, J. Sun, J. Luo, H. L. Xin. *Angew. Chem. Int. Ed.* **60**, 345 (2020).
[85] Y. Huang, T. Yang, L. Yang, R. Liu, G. Zhang, J. Jiang, Y. Luo, P. Lian, S. Tang. *J. Mater. Chem. A.* **7**, 15173 (2019).
[86] S. K. Sahoo, J. Heske, M. Antonietti, Q. Qin, M. Oschatz, T. D. Kühne. *ACS Appl. Energy Mater.* **3**, 10061 (2020).
[87] W. Zang, T. Yang, H. Zou, S. Xi, H. Zhang, X. Liu, Z. Kou, Y. Du, Y. P. Feng, L. Shen, L. Duan, J. Wang, S. J. Pennycook. *ACS Catal.* **9**, 10166 (2019).
[88] Y. H. Wang, A. N. Xu, Z. Y. Wang, L. Huang, J. Li, F. Li, J. Wicks, M. Luo, D.-H. Nam, C.-S. Tan, Y. Ding, J. Wu, Y. Lum, C.-T. Dinh, D. Sinton, G. Zheng, E. H. Sargent. *J. Am. Chem. Soc.* **142**, 5702 (2020).
[89] R. K. Rai, D. Tyagi, S. K. Singh. *Eur. J. Inorg. Chem.* **2017**, 2450 (2017).
[90] R. R. Jia, Y. T. Wang, C. H. Wang, Y. Ling, Y. Yu, B. Zhang. *ACS Catal.* **10**, 3533 (2020).
[91] J. Li, G. M. Zhan, J. H. Yang, F. Quan, C. Mao, Y. Liu, B. Wang, F. Lei, L. Li, A. W. M. Chan, L. Xu, Y. Shi, Y. Du, W. Hao, P. K. Wong, J. Wang, S.-X. Dou, L. Zhang, J. C. Yu. *J. Am. Chem. Soc.* **142**, 7036 (2020).
[92] T. H. Zhu, Q. S. Chen, P. Liao, W. Duan, S. Liang, Z. Yan, C. Feng. *Small* **16**, 2070264 (2020).
[93] H. Niu, Z. F. Zhang, X. T. Wang, X. Wan, C. Shao, Y. Guo. *Adv. Funct. Mater.* **31**, 2008533 (2020).
[94] P. H. v. Langevelde, I. Katsounaros, M. T. M. Koper. *Joule* **5**, 290 (2021).
[95] J. Linnemann, K. Kanokkanchana, K. Tschulik. *ACS Catal.* **11**, 5318 (2021).
[96] J. Li, S. Chen, F. Quan, G. Zhan, F. Jia, Z. Ai, L. Zhang. *Chem* **6**, 885 (2020).